Quantitative Scanning Microwave Microscopy for Transfer Characteristics of GaN High-Electron-Mobility Transistors

Xiaopeng Wang, *Member, IEEE*, Kazuki Nomoto, *Senior Member, IEEE*, Gianluca Fabi, *Member, IEEE*, Marco Farina, *Senior Member, IEEE*, Debdeep Jena, *Fellow, IEEE*, Huili Grace Xing, *Fellow, IEEE*, and James C. M. Hwang, *Life Fellow, IEEE*

***Abstract*— This article demonstrates the feasibility in using a scanning microwave microscope (SMM) to probe the transfer characteristics of an *ungated* GaN high-electron-mobility transistor (HEMT). To guide the experiment and to interpret the result, an equivalent circuit is proposed to model the probe-sample near-field interaction, and the model is validated by simulation and experimentation. In the experiment, the SMM probe with a dc bias voltage acts as a surrogate to locally modulate the 2-D electron gas (2DEG) at the GaN heterojunction. Because the present SMM is most sensitive to a 2DEG sheet resistance R_{SH} between 10^4 Ω/□ and 10^6 Ω/□, the unbiased R_{SH} is determined to be $(3 \pm 3) \times 10^3$ Ω/□, in contrast to ∼450 Ω/□ determined by Hall measurements. However, with the bias decreasing from 0 to −8 V, the 2DEG is depleted and its resistance is increased to $(5 \pm 2) \times 10^5$ Ω/□ with an on/off ratio of 160, a peak transconductance around −5 V, and a threshold voltage of −6 V. These results agree with the dc-measured current–voltage characteristics on a *gated* HEMT after its fabrication is completed. This shows that the SMM could be a powerful tool for in-process monitoring and material/device correlation.**

***Index Terms*— 2-D electron gas (2DEG), GaN high-electron-mobility transistor (HEMT), scanning microwave microscope (SMM), transfer characteristics.**

Manuscript received 18 May 2024; revised 17 July 2024 and 16 August 2024; accepted 20 August 2024. This work was supported in part by the Semiconductor Research Corporation (SRC) and U.S. Defense Advanced Research Projects Agency (DARPA) through the Joint University Microelectronics Program (JUMP); in part by U.S. Army under Grant W911NF-14-1-0665, Grant W911NF-17-1-0090, Grant W911NF-17-P-0073, Grant W911NF-18-C-0094, and Grant W911NF-24-1-0023; in part by U.S. Air Force under Grant FA9550-16-1-0475, Grant FA9550-17-1-0043, and Grant FA9550-20-1-0148; in part by U.S. National Science Foundation under Grant 1433459-EFMA, Grant 1710298, and Grant 2132323; in part by the Cornell NanoScale Facility, an National Nanotechnology Coordinated Infrastructure (NNCI) member supported by NSF, under Grant NNCI-2025233; and in part by the Cornell Center for Materials Research Shared Facilities through NSF Materials Research Science and Engineering Centers (MRSEC) Program under Grant DMR-1719875. *(Corresponding author: Xiaopeng Wang.)*

Xiaopeng Wang, Kazuki Nomoto, and Gianluca Fabi are with the School of Electrical and Computer Engineering, Cornell University, Ithaca, NY 14850 USA (e-mail: xw569@cornell.edu).

Marco Farina is with the Department of Information Engineering, Marche Polytechnical University, 60131 Ancona, Italy.

Debdeep Jena, Huili Grace Xing, and James C. M. Hwang are with the School of Electrical and Computer Engineering and the Department of Materials Science and Engineering, Cornell University, Ithaca, NY 14850 USA.

Color versions of one or more figures in this article are available at https://doi.org/10.1109/TMTT.2024.3449128.

Digital Object Identifier 10.1109/TMTT.2024.3449128

I. Introduction

THE scanning microwave microscope (SMM) has been proven as a metrology tool, including the characterization of semiconductors, dielectrics, and biological cells [1], [2], [3], [4], [5]. Typically, in an SMM, a metal probe is scanned across the sample surface with the height controlled through the feedback of force as in an atomic force microscope (AFM). Meanwhile, a microwave signal is injected through the probe, and the magnitude and phase of the signal reflected from the sample are the characteristic of the electromagnetic properties of the sample. Unlike the AFM, the SMM can sense the properties of buried structures below the surface [6], [7], [8], [9], [10], [11], such as the 2-D electron gas (2DEG) at an AlN/GaN heterojunction.

GaN high-electron-mobility transistors (HEMTs) have high breakdown voltage, high carrier density, and high electron saturation velocity [12], [13], [14]. These attributes make GaN HEMTs attractive to next-generation wireless communications, including applications in high-power amplifiers, low-noise amplifiers, and other integrated circuits [15], [16], [17]. To facilitate these applications, the electrical properties of the HEMT heterostructure need to be constantly characterized. Typically, Hall measurement or contactless resistivity mapping [18] is used to characterize the heterostructure before device fabrication, and the dc current–voltage measurement is used to characterize the HEMT device after fabrication. However, when these measurements do not agree with each other, it is not obvious when the heterostructure properties are degraded during fabrication. Usually, the Hall measurement is destructive, and the contactless resistivity mapping requires bare wafers and achieves only millimeter resolution, making them unsuitable for in-process monitoring. Similarly, the dc measurements, averaged over the entire HEMT, lack spatial resolution for the characterization of material nonuniformity on the nanoscale.

In this work, we show that the SMM, with a biased probe, can be used to nondestructively measure the local 2DEG sheet resistivity and transfer characteristics during the HEMT fabrication process. The SMM also reveals localized defects in the HEMT channel with submicrometer spatial resolution.

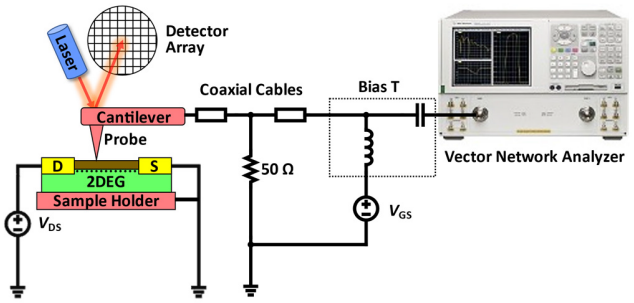

Fig. 1. Schematics of an AFM-based SMM.

II. Experimental Setup

Fig. 1 illustrates the present experimental setup based on a Keysight Technologies 7500 AFM with an N9545C SMM nose cone. The AFM/SMM dual-function probe is a Rocky Mountain 25Pt300A platinum probe having a spring constant of 18 N/m. The probe is attached to a 300-μm-long, 60-μm-wide, and 2-μm-thick platinum cantilever. The cantilever, in turn, is connected to a Keysight Technologies E8062B vector network analyzer (VNA) through coaxial cables. The cables are shunted by a 50-Ω resistor for impedance matching around 3 GHz and its harmonics. This resistor is rated for 2 W. Therefore, even under a bias as negative as −8 V, no significant heating or bias drift is experienced.

The VNA generates a 0-dBm signal at 12.97 GHz, which is emitted from the probe. The 0-dBm power provides adequate signal-to-noise ratio (SNR) yet is minimally invasive. The 12.97-GHz frequency is chosen for its maximum imaging contrast. Following near-field interaction with the sample, the signal reflected back through the probe is also detected by the VNA. The intermediate frequency bandwidth of the VNA is set at 500 Hz, trading off the SNR for the scan rate. With a scan rate of 200 pixel/s, it takes approximately 4 min to scan a 15 × 15 μm area with a resolution of 256 × 256 pixels. A Keysight Technologies E3620A dual-output dc power supply provides a gate–source voltage V_{GS} through a Keysight 11612A bias T to the probe and a drain–source voltage V_{DS} through a bond wire to the drain electrode of the HEMT (Fig. 2).

To increase the sensitivity to the 2DEG sheet resistance R_{SH}, a relatively large probe is used at the expense of spatial resolution. The probe is scanned across the sample in a contacting mode with a force of approximately 200 nN applied through the piezoelectric stage and sensed by the cantilever deflection. Assuming the probe tip is a half sphere and the probe body is a truncated cone, the probe geometry can be calibrated by the measured capacitance-height dependence as the probe approaches a grounded metal sample holder [19], [20], [21]. Thus, by fitting the reflection coefficient measured as a function of the height above the holder, it is determined that the probe tip has a radius $r = 0.4$ μm, and the probe body has a height $h = 60$ μm and a half cone angle $\theta = 20°$. According to [19], [20], and [21], the uncertainty in r has the greatest impact on the SMM conductance and capacitance contrasts. In the present case, the resulted uncertainty in the SMM conductance/capacitance contrasts is approximately 3%,

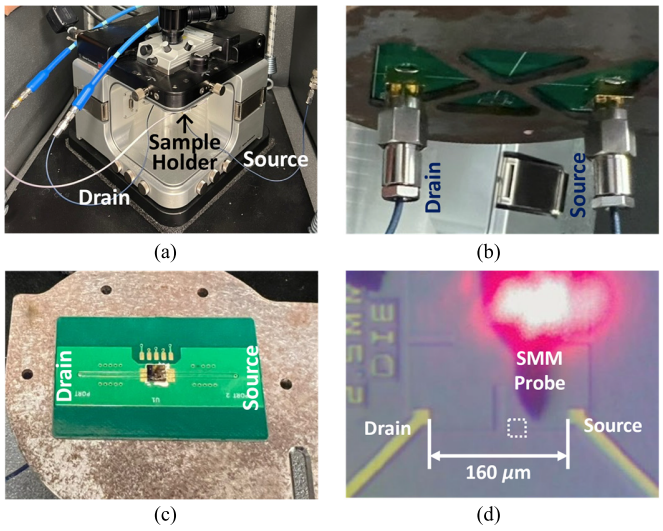

Fig. 2. (a) SMM sample chamber showing the sample holder mounted on the ceiling of the chamber in contact with the SMM nose cone. (b) Bottom of sample holder showing coaxial cables interconnected through the sample holder to the source and drain transmission lines on the top. (c) Top of sample holder showing an ungated HEMT chip attached to the source and drain transmission lines. (d) Micrograph showing the scanned area (dotted) with respect to the source and drain electrodes of an ungated HEMT wire bonded to the transmission lines.

which is negligible compared to the overall uncertainty in the extracted R_{SH}.

The HEMT heterostructure is grown by a commercial supplier on a 700-μm-thick high-resistivity Si substrate using metal–organic chemical vapor deposition without doping. With their wide bandgaps, the intrinsic carrier density at room temperature is negligible and these undoped nitrides can be treated as dielectrics, such as high-resistivity Si and semi-insulating GaAs. As shown in Fig. 3(a), the growth starts with a 100-nm AlN nucleation layer, which is followed by a 500-nm AlGaN buffer layer, an 800-nm GaN channel layer, a 1-nm AlN barrier layer, and finally, a 10-nm $In_{0.17}Al_{0.83}N$ cap layer. Consequently, the 2DEG is induced by piezoelectric doping [22] 11 nm below the surface at the AlN/GaN heterojunction. During the HEMT fabrication, the 2DEG regions are isolated by dry etching to a depth of 200 nm, and 40/200-nm-thick Ni/Au source and drain electrodes are formed before the SMM scan. Normally, the source–drain spacing is 2 μm. However, for the proof of concept, a "fat" HEMT with a channel area of 100 × 200 μm between the source and drain is chosen to ensure the relatively large SMM probe is not impeded by the source and drain electrodes.

Fig. 3(b) shows the AFM topography image and line scan from the active region (with 2DEG) to the isolated region (without 2DEG). The spots in the isolated region are debris accidentally left by the fabrication process. They serve as landmarks to ensure the same area is scanned by the SMM repeatedly.

III. Modeling and Simulation

To guide the experiment and to interpret the result, a simple equivalent circuit model is first developed. It is then validated by numerical simulation. Following most quantitative SMM

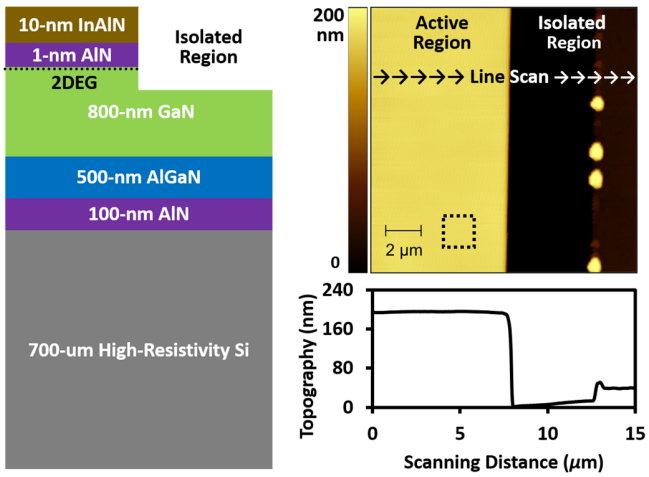

(a) (b)

Fig. 3. (a) HEMT cross section schematics. (b) AFM topography image and line scan from the active region to the isolated region.

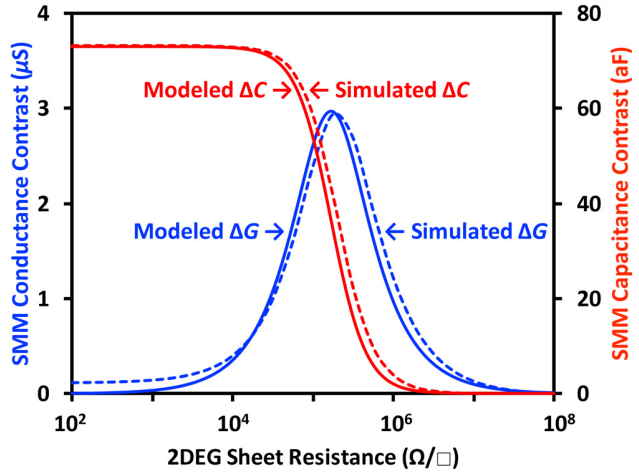

Fig. 4. Modeled (solid curves) versus simulated (dashed curves) conductance and capacitance contrasts as functions of 2DEG sheet resistance R_{SH}.

studies, we solve the inverse problem by first assuming different values of the 2DEG sheet resistance and calculate/simulate the SMM conductance/capacitance contrasts, as shown in Fig. 4. We then compare the modeled/simulated conductance/capacitance contrasts to that measured in order to extract R_{SH}. In short, R_{SH} is fitted to the data instead of derivation from the data, typical of quantitative SMM studies. As detailed in the following, the uncertainty in the extracted R_{SH} caused by the limited sensitivity of the SMM does not justify more complicated modeling or analysis. This fitting approach is validated by comparing the extracted R_{SH} with that measured by the Hall effect, as described in Section IV-A.

A. Equivalent Circuit Model

In contrast to conventional equivalent circuit models [23], we propose a three-element equivalent circuit of different topologies for the present sample, as shown in Fig. 5. This is because the 2DEG in the HEMT channel is ohmic-connected to the source and drain electrodes with a channel resistance of R_0 [14], and it acts as a ground plane to shield the electrical

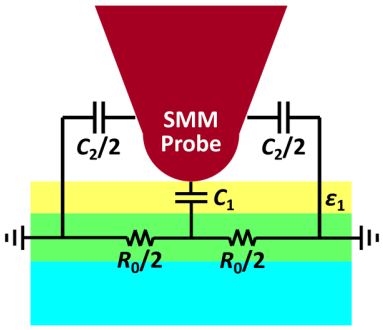

Fig. 5. Equivalent circuit model with the ground plane in the middle of the sample.

field from penetrating below the 2DEG. C_1 represents all layers of the heterostructure above the 2DEG with their respective dielectric constant and thickness. The layers below the 2DEG are immaterial. C_2 represents the fringing capacitance between the probe body and the sample. Thus

$$Y = G + j\omega C = \frac{j\omega G_0 C_1}{G_0 + j\omega C_1} + j\omega C_2 \tag{1}$$

where $G_0 = 1/R_0$ and the second term $j\omega C_2$ dominates the interaction admittance when the SMM is scanned over the isolated region. Therefore, the admittance contrast between the active and isolated regions is

$$\Delta Y = \frac{j\omega G_0 C_1}{G_0 + j\omega C_1} \tag{2}$$

and the conductance contrast ΔG and capacitance contrast ΔC are

$$\Delta G = \frac{G_0 \omega^2 C_1^2}{G_0^2 + \omega^2 C_1^2} \tag{3}$$

and

$$\Delta C = \frac{G_0^2 C_1}{G_0^2 + \omega^2 C_1^2}. \tag{4}$$

As expected, $\Delta G \approx G_0$ if $R_0 \gg \omega C_1$ and $\Delta C \approx C_1$ if $R_0 \ll \omega C_1$. Meanwhile, $\Delta G \approx 0$ if $R_0 \ll \omega C_1$ and $\Delta C \approx 0$ if $R_0 \gg \omega C_1$. In between the extremes, ΔG peaks when $R_0 C_1 = 1/\omega$, whereas ΔC monotonically decreases from C_1 to 0. Therefore, ΔC is the most sensitive to R_0 when $R_0 = 1/\omega C_1$, whereas ΔG is the most sensitive to R_0 when R_0 is slightly larger or smaller than $1/\omega C_1$. In other words, for sensitivity, the SMM frequency should match the inverse of the $R_0 C_1$ time constant. Giving a fixed $\omega = 2\pi \cdot 12.97$ GHz, the probe can be biased to partially deplete the 2DEG so that $R_0 \approx 1/\omega C_1 \approx 10^5\ \Omega$ for high sensitivity. From ΔC when $V_{GS} = 0$, $C_1 = 73$ aF. Fig. 4 plots (3) and (4) as functions of R_0.

B. Numerical Simulation

Three-dimensional finite-element electromagnetic simulation is performed by using the COMSOL ac/dc module. Quasi-static approximation is invoked because the wavelength in GaN around 10 GHz is on the order of 1 cm, which is significantly longer than the SMM probe diameter or the HEMT heterostructure thickness. To simply the heterostructure

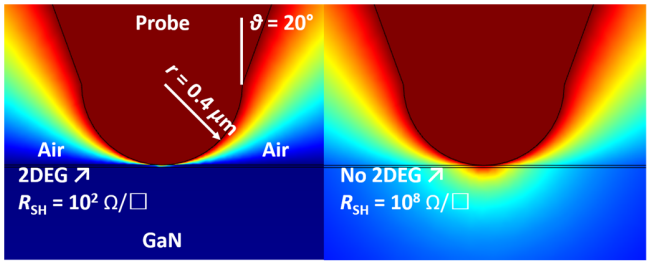

Fig. 6. Simulated electrical potential distribution around the SMM probe (left) with and (right) without the 2DEG.

for simulation, the InAlN and AlN layers above the 2DEG are assumed to have the same dielectric constant of 8.5, while all other layers above silicon are assumed to have a dielectric constant of 8.9 [24]. According to [24], ignoring the difference in dielectric constants of AlN, GaN, and their alloys has negligible impact on the SMM conductance/capacitance contrasts. The 2DEG is modeled by an electric-shielding boundary condition with a sheet resistance R_{SH} and an equivalent thickness of 2 nm. The round 2DEG area in interaction with the SMM probe can be approximated by a square, so that $R_{SH} \approx R_0$ [25]. Fig. 6 shows the simulated potential distribution with 2DEG ($R_{SH} = 10^2$ Ω/□) and without 2DEG ($R_{SH} = 10^8$ Ω/□). It can be seen that the 2DEG is an effective ground plane preventing the electric field from extending below it. The simulated ΔG and ΔC agree with those modeled by the equivalent circuit, as shown in Fig. 4. The small difference in ΔG when $R_{SH} \approx 0$ is irrelevant because there ΔG is independent of R_{SH} and, hence, cannot be used to extract R_{SH}.

IV. Results and Discussion

A. Biased SMM

To locally modulate the 2DEG of an ungated HEMT by the SMM probe, V_{GS} is applied to the probe from 0 to −8 V then back to 0 in 1-V steps while V_{DS} is kept at 1 V. The bias leaves no lasting effect because the first and last scans without bias give similar results. The measured reflection coefficients under each bias are used to extract the interaction admittance Y between the SMM probe and the 2DEG [19], [20], [21], as well as ΔY, ΔG, and ΔC. It can be seen in Fig. 7 that as V_{GS} decreases, ΔG appears to peak around −6 V while ΔC monotonically decreases, qualitatively in agreement with both modeled and simulated behaviors shown in Fig. 4.

By quantitatively fitting the measured ΔG and ΔC with (3) and (4), R_{SH} can be extracted (Fig. 8) after subtracting from as-measured ΔC the topography crosstalk ΔC_P, which originates from the different heights of the active and isolated regions [21]. Even with exactly the same heterostructure and R_{SH} in both regions, when the SMM probe is elevated by 200 nm, the change in the fringing capacitance ΔC_P will be recorded as part of ΔC. ΔC_P has hitherto not been considered in either the equivalent circuit model or numerical simulation, because it can only be experimentally determined. Since the as-measured $\Delta C = 18$ aF when $V_{GS} = -8$ V, $\Delta C_P = 18$ aF because the 2DEG channel is depleted and there should be no contrast between active and isolated regions. The topography crosstalk has negligible effect on ΔG.

Thus, when $V_{GS} = 0$, $\Delta G = 0.2 \pm 0.2$ μS and $\Delta C = 73 \pm 5$ aF. Hence, $R_{SH} = (3 \pm 3) \times 10^3$ Ω/□ (Fig. 8). This R_{SH} value can be order-of-magnitude higher than the sheet resistance of 450 Ω/□ measured by the Hall effect, reflecting the limited sensitivity of ΔG and ΔC to R_{SH} when $R_{SH} < 10^4$ Ω/□. On the other hand, when $V_{GS} = -5$ V, ΔG increases to 1.4 ± 0.2 μS, while ΔC decreases to 52 ± 6 aF. With R_{SH} approaching $1/\omega C_1$, the sensitivity is increased, so that $R_{SH} = (9 \pm 3) \times 10^4$ Ω. When V_{GS} is decreased from −6 to −8 V, ΔG decreases from 1.9 ± 0.2 to 1.5 ± 0.2 μS, while intrinsic ΔC decreases from 15 ± 4 to 0 ± 3 aF. Consequently, $R_{SH} = (5 \pm 1)$, (6 ± 1), and $(8 \pm 2) \times 10^5$ Ω for $V_{GS} = -6$, −7, and −8 V, respectively. Across different V_{GS} values, the standard deviations in ΔG and ΔC remain approximately constant around 0.3 μS and 4 aF, respectively. In fact, the standard deviation in $\omega\Delta C$ is comparable to the standard deviation in ΔG, reflecting the noise floor of the present measurement setup.

B. Defects in 2DEG

In addition to extracting R_{SH}, the SMM can resolve defects in 2DEG with submicrometer spatial resolution. Despite the uniformity in ΔG and ΔC in most cases (Fig. 7), localized defects can be seen in the ΔG and ΔC images with $V_{GS} = -5$ V just before the 2DEG is fully depleted. For example, the dotted area in Fig. 7 containing two adjacent defects is zoomed in, as shown in Fig. 9. It can be seen that the conductance is ∼0.3 μS higher, while the intrinsic capacitance is ∼20 aF lower inside the defects than that outside the defects, implying lower R_{SH}. The diameter of the defects appears to be approximately 1/3 μm, which reflects the SMM probe size. Even with a sharper SMM probe, what is measured is the electrical influence zone of the defects. Their physical structure may be much smaller in any case. Moreover, the depth at which the defect is located will affect the maximum achievable resolution of the SMM, regardless of the probe size. Meanwhile, no topography contrast can be seen by the AFM on the surface above the defects [Fig. 9(a)]. To illustrate this point, ΔG and ΔC inside a defect are compared with that outside the defect as functions of V_{GS} (Fig. 10). It can be seen that the defect region has not only a less negative threshold voltage but also a less steep subthreshold slope. The defect density is on the order of 10^8/cm^2.

Among all possible defects, such as process defects, we speculate that the defects observed by SMM are caused by threading dislocations and, in particular, screw dislocations threading through the HEMT heterostructure. It has been reported that the density of GaN heterostructure is on the order of 10^9/cm^2 [26]. However, of all threading dislocations, typically up to one third are screw dislocations or mixed screw-edge dislocations. Compared to edge dislocations, screw dislocations tend to be larger spatially and electrically and to induce a larger quantity of deep traps. This implies that of all threading dislocations, only 10^8 cm^2 matter electrically, in agreement with the SMM observation. Note that normally

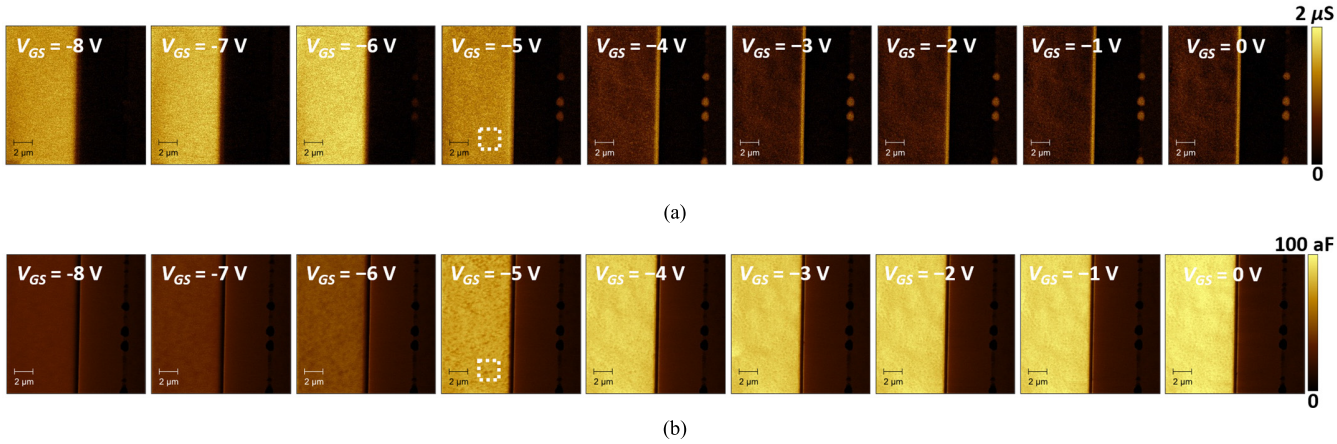

Fig. 7. SMM-measured (a) conductance contrasts and (b) capacitance contrasts on an ungated HEMT with the SMM probe biased under different V_{GS} values.

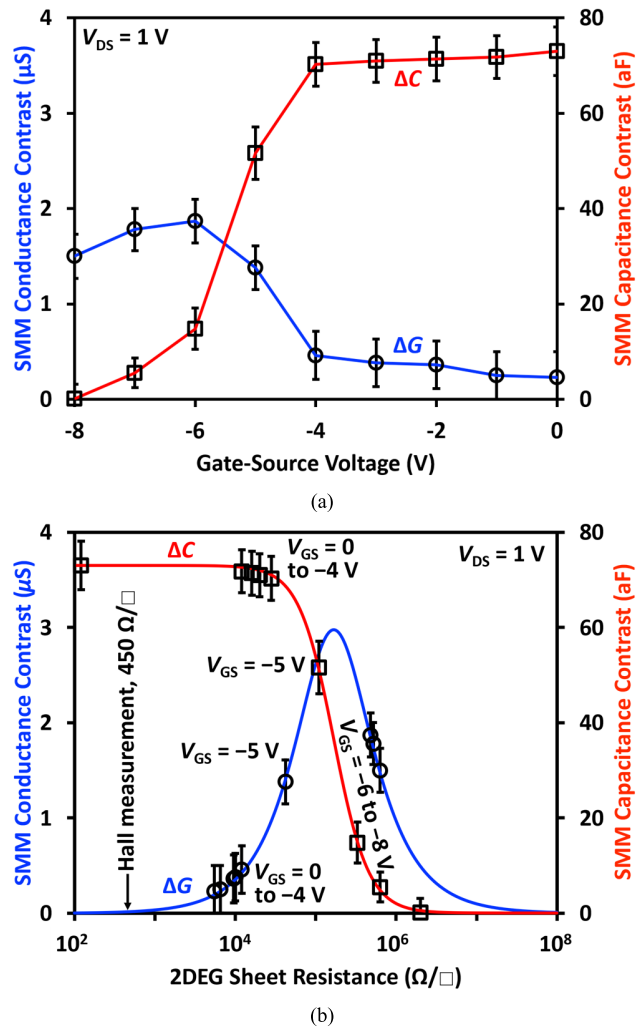

Fig. 8. SMM-measured conductance contrast (○) and capacitance contrast (□) as functions of (a) V_{GS} and (b) R_{SH}.

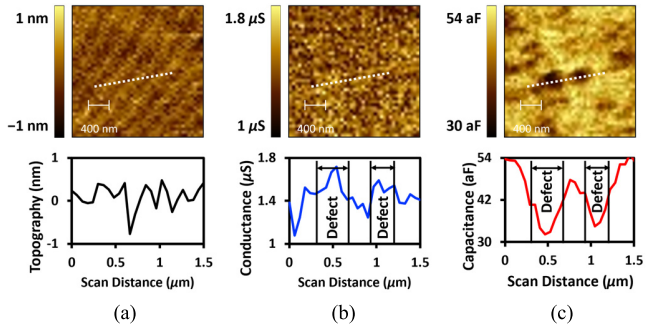

Fig. 9. Zoomed-in images of (a) AFM topography contrast, (b) SMM conductance contrast, and (c) SMM capacitance contrast around two defects, as well as linear scans along the dotted lines across the defects.

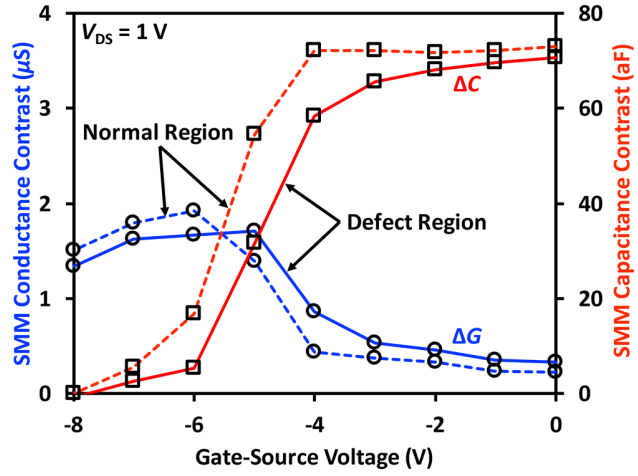

Fig. 10. SMM-measured conductance and capacitance contrasts inside (solid) and outside (dashed) the defect region as functions of V_{GS}.

threading dislocations can also be observed structurally by AFM. However, when the present large probe is used for simultaneous AFM/SMM, it may not have sufficient spatial resolution for the threading dislocations structurally by AFM. The large probe also makes it difficult for SMM to electrically resolve a dislocation density as high as 10^9/cm^2.

Presently, the SMM spatial resolution is limited by the probe size, which, in turn, is limited by the SMM sensitivity. The present analysis shows that the maximum sensitivity is achieved when $R_{SH} \approx 1/\omega C_1$. Although a smaller probe makes C_1 smaller, it can be compensated by a higher ω. By changing the VNA and the coaxial cables, we have incrementally

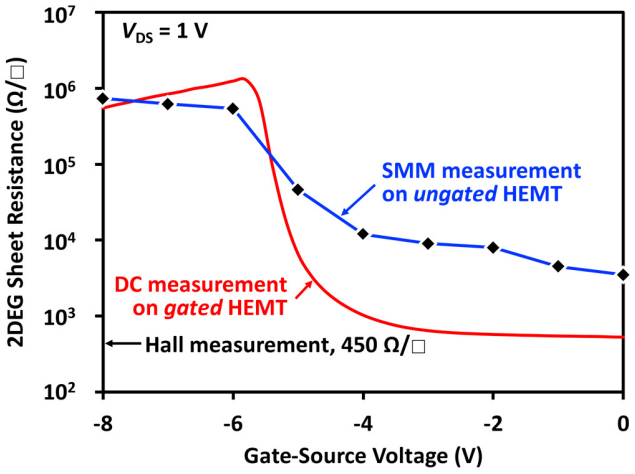

Fig. 11. Transfer characteristics measured by the SMM on an *ungated* HEMT versus that by the dc measurement on a gated HEMT.

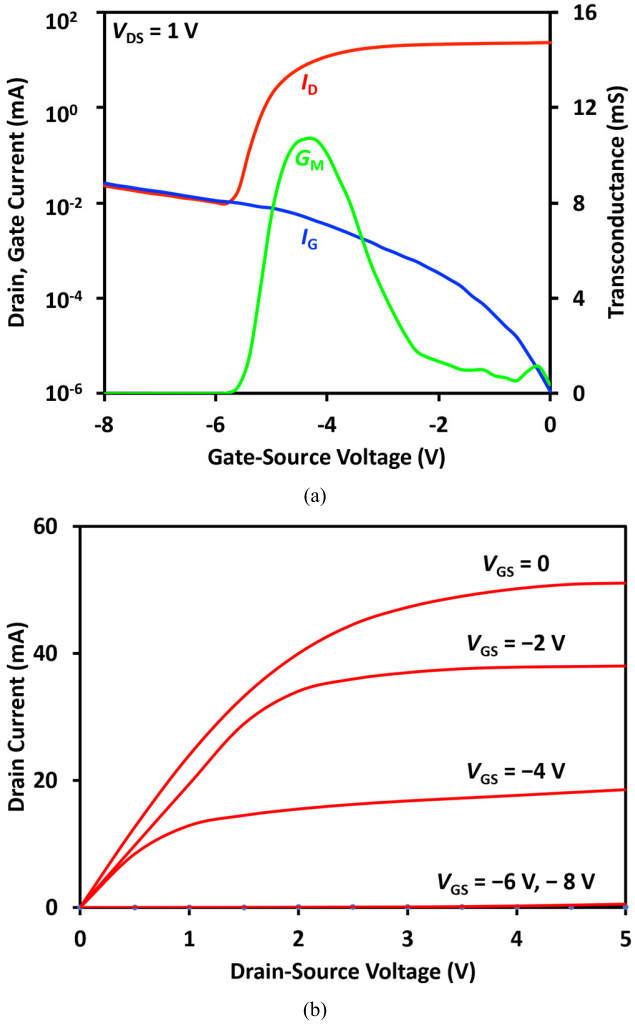

Fig. 12. (a) Transfer and (b) output characteristics measured on a *gated* HEMT by the dc measurement.

improved the SMM bandwidth above 10 GHz as in the present 12.97-GHz case. Most recently, we have further improved the bandwidth to 15 GHz. For order-of-magnitude improvement of the SMM bandwidth, major modifications of the setup, as in the case of an inverted SMM [27], are needed. For example, to confidently resolve $R_{SH} \sim 500$ Ω/□, a frequency of 75 GHz is required using the same probe size.

C. Transfer Characteristics

Fig. 11 compares the transfer characteristic measured by the SMM on the *ungated* HEMT with that by the dc measurement on a *gated* HEMT with the same heterostructure. The *gated* HEMT has a gate length of 2 μm and a gate width of 25 μm. It can be seen that the characteristics generally follow each other, and both indicate a threshold voltage between −5 and −6 V. However, the SMM-measured R_{SH} is lower above the threshold, resulting in order-of-magnitude lower on/off ratio when compared to the dc-measured value of $\sim 10^3$. This shows the limited dynamic range of the present SMM. As illustrated in Fig. 4, the SMM is sensitive to R_{SH} only from 10^4 to 10^6 Ω/□.

For the sake of completeness, Fig. 12 shows the dc-measured transfer and output characteristics of the gated HEMT. It can be seen that, above the threshold voltage, the drain current I_D is orders-of-magnitude higher than the gate current I_G. However, even with V_{GS} decreased to −8 V, I_G appears to saturate around 10 μA as for a normal Schottky contact without any sign of breakdown.

V. Conclusion

An SMM probe, when biased with a dc voltage, can act as a surrogate for local modulation and characterization of the 2DEG in a GaN HEMT heterostructure. In this case, the interaction between the SMM probe and the 2DEG can be modeled by a simple equivalent circuit, which is validated by finite-element simulation and experimental measurement. Guided by the model, the HEMT channel resistance and transfer characteristics have been quantitatively characterized and correlated to that measured on the HEMT after its fabrication is completed. Defects in 2DEG are revealed by the SMM but not by the AFM or dc measurement. Thus, the SMM can be used as a powerful in-process monitor for material/device correlation.

Acknowledgment

The content of the information does not necessarily reflect the position or the policy of the federal government, and no official endorsement should be inferred.

References

[1] R. C. Chintala, K. Rubin, and Y. Yang, "Scanning microwave impedance microscopy: Room-temperature and low-temperature applications for device and material characterization," *IEEE Microw. Mag.*, vol. 21, no. 10, pp. 22–35, Oct. 2020.

[2] S. Berweger, T. M. Wallis, and P. Kabos, "Nanoelectronic characterization: Using near-field microwave microscopy for nanotechnological research," *IEEE Microw. Mag.*, vol. 21, no. 10, pp. 36–51, Oct. 2020.

[3] M. Farina and J. C. M. Hwang, "Scanning microwave microscopy for biological applications: Introducing the state of the art and inverted SMM," *IEEE Microw. Mag.*, vol. 21, no. 10, pp. 52–59, Oct. 2020.

[4] L. Zheng, L. Shao, M. Loncar, and K. Lai, "Imaging acoustic waves by microwave microscopy: Microwave impedance microscopy for visualizing gigahertz acoustic waves," *IEEE Microw. Mag.*, vol. 21, no. 10, pp. 60–71, Oct. 2020.

[5] A. Tselev, "Near-field microwave microscopy: Subsurface imaging for in situ characterization," *IEEE Microw. Mag.*, vol. 21, no. 10, pp. 72–86, Oct. 2020.

[6] K. Lai, W. Kundhikanjana, M. A. Kelly, Z.-X. Shen, J. Shabani, and M. Shayegan, "Imaging of Coulomb-driven quantum Hall edge states," *Phys. Rev. Lett.*, vol. 107, no. 17, Oct. 2011, Art. no. 176809.

[7] E. Y. Ma et al., "Unexpected edge conduction in mercury telluride quantum wells under broken time-reversal symmetry," *Nature Commun.*, vol. 6, no. 1, p. 7252, May 2015.

[8] G. Gramse et al., "Nondestructive imaging of atomically thin nanostructures buried in silicon," *Sci. Adv.*, vol. 3, no. 6, Jun. 2017, Art. no. e1602586.

[9] W. Choi et al., "Direct electrical probing of periodic modulation of zinc-dopant distributions in planar gallium arsenide nanowires," *ACS Nano*, vol. 11, no. 2, pp. 1530–1539, Feb. 2017.

[10] M. Allen et al., "Visualization of an axion insulating state at the transition between 2 chiral quantum anomalous Hall states," *Proc. Nat. Acad. Sci. USA*, vol. 116, no. 29, pp. 14511–14515, Jul. 2019.

[11] S. Berweger et al., "Imaging of magnetic excitations in nanostructures with near-field microwave microscopy," *J. Magn. Magn. Mater.*, vol. 546, Mar. 2022, Art. no. 168870.

[12] A. Hickman et al., "First RF power operation of AlN/GaN/AlN HEMTs with > 3 A/mm and 3 W/mm at 10 GHz," *IEEE J. Electron Devices Soc.*, vol. 9, pp. 121–124, 2021.

[13] S. J. Bader et al., "Prospects for wide bandgap and ultrawide bandgap CMOS devices," *IEEE Trans. Electron Devices*, vol. 67, no. 10, pp. 4010–4020, Oct. 2020.

[14] L. Li et al., "GaN HEMTs on Si with regrown contacts and cutoff/maximum oscillation frequencies of 250/204 GHz," *IEEE Electron Device Lett.*, vol. 41, no. 5, pp. 689–692, May 2020.

[15] L. Li, P. Fay, and J. C. M. Hwang, "A D-band frequency-doubling traveling-wave amplifier through monolithic integration of a SiC SIW and GaN HEMTs," *IEEE J. Microw.*, vol. 4, no. 1, pp. 158–166, Jan. 2024.

[16] F. Thome, P. Brückner, and R. Quay, "A D-Band low-noise amplifier MMIC in a 70-nm GaN HEMT technology," in *Proc. 18th Eur. Microw. Integr. Circuits Conf. (EuMIC)*, Berlin, Germany, Sep. 2023, pp. 5–8.

[17] F. Thome, D. Schwantuschke, P. Brückner, X. Wang, J. C. M. Hwang, and R. Quay, "A < 5 dB NF, > 17 dBm OP1 dB F-band GaN-on-SiC HEMT LNA with a monolithic substrate-integrated waveguide filter," in *IEEE MTT-S Int. Microw. Symp. Dig.*, Jun. 2024, pp. 314–317.

[18] J. Krupka, D. Nguyen, and J. Mazierska, "Microwave and RF methods of contactless mapping of the sheet resistance and the complex permittivity of conductive materials and semiconductors," *Meas. Sci. Technol.*, vol. 22, no. 8, Jul. 2011, Art. no. 085703.

[19] M. Farina, D. Mencarelli, A. Di Donato, G. Venanzoni, and A. Morini, "Calibration protocol for broadband near-field microwave microscopy," *IEEE Trans. Microw. Theory Techn.*, vol. 59, no. 10, pp. 2769–2776, Oct. 2011.

[20] G. Gramse, M. Kasper, L. Fumagalli, G. Gomila, P. Hinterdorfer, and F. Kienberger, "Calibrated complex impedance and permittivity measurements with scanning microwave microscopy," *Nanotechnology*, vol. 25, no. 14, Apr. 2014, Art. no. 145703.

[21] X. Jin, M. Farina, X. Wang, G. Fabi, X. Cheng, and J. C. M. Hwang, "Quantitative scanning microwave microscopy of the evolution of a live biological cell in a physiological buffer," *IEEE Trans. Microw. Theory Techn.*, vol. 67, no. 12, pp. 5438–5445, Dec. 2019.

[22] O. Ambacher et al., "Two-dimensional electron gases induced by spontaneous and piezoelectric polarization charges in N-and Ga-face AlGaN/GaN heterostructures," *J. Appl. Phys.*, vol. 85, no. 6, pp. 3222–3233, Mar. 1999.

[23] S. M. Anlage, V. V. Talanov, and A. R. Schwartz, "Principles of near-field microwave microscopy," in *Scanning Probe Microscopy: Electrical and Electromechanical Phenomena at the Nanoscale*. New York, NY, USA: Springer, 2007, pp. 215–253.

[24] X. Wang et al., "Quantitative scanning microwave microscopy of 2D electron and hole gases in AlN/GaN heterostructures," *Appl. Phys. Lett.*, vol. 120, no. 1, Jan. 2022, Art. no. 012103.

[25] K. Seki, T. Kubo, N. Ye, and T. Shimizu, "Quantifying the spreading resistance of an anisotropic thin film conductor," *Sci. Rep.*, vol. 10, no. 1, p. 10633, Jun. 2020.

[26] O. Laboutin et al., "The resurgence of III-N materials development: AlInN HEMTs and GaN-on-Si," *ECS Trans.*, vol. 41, no. 8, pp. 301–311, Oct. 2011.

[27] M. Farina et al., "Inverted scanning microwave microscope for in vitro imaging and characterization of biological cells," *Appl. Phys. Lett.*, vol. 114, no. 9, Mar. 2019, Art. no. 093703.

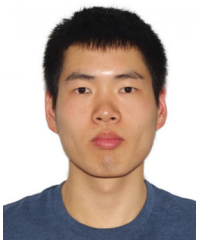

Xiaopeng Wang (Member, IEEE) received the B.S. degree in information engineering from Xi'an Jiaotong University, Xi'an, China, in 2015, the M.S. degree in electrical engineering from Lehigh University, Bethlehem, PA, USA, in 2017, and the Ph.D. degree in electrical and computer engineering from Cornell University, Ithaca, NY, USA, in 2024.

His current research interests include scanning microwave microscopy, substrate-integrated waveguides, low-noise amplifiers, monolithic and heterogeneous integration of antennas, filters, and HEMTs for sub-THz integrated circuits.

Kazuki Nomoto (Senior Member, IEEE) received the B.S., M.S., and Ph.D. degrees in electrical engineering from Hosei University, Tokyo, Japan, in 2004, 2006, and 2009, respectively.

He has been with the School of Electrical and Computer Engineering, Cornell University, Ithaca, NY, USA, since 2015, where he has been involved in the research and development of wide bandgap semiconductor power devices.

Gianluca Fabi (Member, IEEE) received the B.S. degree in electronics engineering from Marche Polytechnic University, Ancona, Italy, in 2015, the M.S. degree in electronics engineering from Politecnico di Torino, Turin, Italy, in 2017, and the Ph.D. degree from the Department of Information Engineering, Marche Polytechnic University, in 2021.

After that, he is a Post-Doctoral Researcher with the Department of Information Engineering and the Department of Electrical and Computer Engineering, Cornell University, Ithaca, NY, USA. His research focuses on microwave measurements, devices, and characterization techniques.

Marco Farina (Senior Member, IEEE) received the M.S. and Ph.D. degrees in electronic engineering from Marche Polytechnic University, Ancona, Italy, in 1990 and 1995, respectively.

He is currently a Professor of electromagnetics with Marche Polytechnic University. He has authored the electromagnetic simulation software EM3DS and is used by a number of institutions and companies for research and design work. He designed and realized a hybrid scanning tunneling microscope/scanning microwave microscope. His research interests include electromagnetic modeling of passive and active structures, scanning probe microscopy, nanotechnology, and measurement techniques.

Dr. Farina is a Technical Committee Member of the IEEE MTT Society TC-25 RF-Nanotechnology.

Debdeep Jena (Fellow, IEEE) received the Ph.D. degree in electrical and computer engineering from the University of California at Santa Barbara (UCSB), Santa Barbara, CA, USA, in 2003.

He is the David E. Burr Professor of engineering with Cornell University, Ithaca, NY, USA. He is with the Departments of Electrical and Computer Engineering and Materials Science and Engineering and is a Field Member with the Department of Applied and Engineering Physics. In 2015, he joined Cornell University and a Faculty Member at Notre Dame, Notre Dame, IN, USA, in August 2003. His teaching and research are in the quantum physics of semiconductors and electronic and photonic devices based on quantized semiconductor structures (e.g., nitrides, oxides, 2-D materials), and their heterostructures with superconductors, ferroelectrics, and magnets, with device applications in energy-efficient transistors, light-emitting diodes and RF and power electronics and quantum computation and communications. His research is driven by the goal to enable orders of magnitude increase in the energy efficiency and speed for computation, memory, communications, lighting, and electrical energy management ranging from the chip to the grid.

Huili Grace Xing (Fellow, IEEE) received the bachelor's degree in physics from Peking University, Beijing, China, in 1996, the master's degree in material science and engineering from Lehigh University, Bethlehem, PA, USA, in 1998, and the Ph.D. degree in electrical engineering from the University of California at Santa Barbara, Santa Barbara, CA, USA, in 2003.

From 2004 to 2014, she was a Faculty Member with the University of Notre Dame, Notre Dame, IN, USA. In 2015, she joined Cornell University, Ithaca, NY, USA. She is currently the William L. Quackenbush Professor of electrical and computer engineering with Cornell University, where she holds a joint appointment with the School of Electrical and Computer Engineering and the Department of Materials Science and Engineering. Her research work can be loosely categorized into four areas of high-performance materials and devices: III–V nitrides, oxides, low-dimensional materials and quantum materials, and logic and memory.

James C. M. Hwang (Life Fellow, IEEE) received the B.S. degree in physics from National Taiwan University, Taipei, Taiwan, in 1970, and the M.S. and Ph.D. degrees in materials science and engineering from Cornell University, Ithaca, NY, USA, in 1976 and 1978, respectively.

From 1988 to 2019, he was a Professor of electrical engineering and the Director of Compound Semiconductor Technology Laboratory, Lehigh University, Bethlehem, PA, USA. Prior to that, he spent 12 years at IBM, AT&T, GE, and GAIN. He is currently a Professor with the same department. He co-founded GAIN and QED; the latter became a public company (IQE). He has worked on electronic, optoelectronic, and micro-electromechanical materials, devices, and circuits for four decades.

Dr. Hwang has received many honors and awards, including the IEEE EDS Lester F. Eastman Award for outstanding achievements in high-performance semiconductor devices.